Graphical Abstract

Capacitive Imaging applied for In-Situ Powder Topographic Characterization during Powder Bed Fusion

Victor Macedo, Jorge Assis, André Barrancos, Luis Rosado

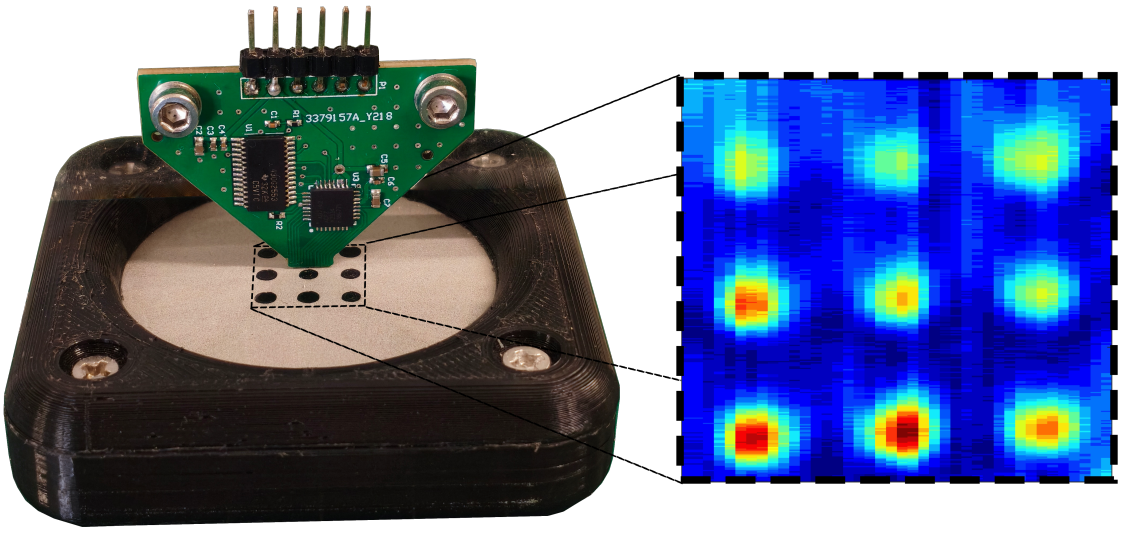

Capacitive Imaging applied for In-Situ Powder Topographic Characterization during Powder Bed Fusion

Victor Macedo[a], Jorge Assis[a], André Barrancos[a,b], Luis Rosado[a,b]

[a]*Instituto Superior Técnico, Universidade de Lisboa, Av. Rovisco Pais 1, 1049-011, Lisboa, Portugal*
[b]*Instituto de Telecomunicações, Av. Rovisco Pais 1, 1049-011, Lisboa, Portugal*

Abstract

Capacitive imaging is proposed for topographic characterization of the surface of successive powder layers during powder bed fusion additive manufacturing. This capability enables new opportunities for early detection and, ultimately, prevention of defective conditions by using extensive capacitive sensor arrays integrated into the recoater unit. Finite element modeling was used to simulate individual capacitive sensors in order to identify a suitable geometry for implementation in an array. A 12 sensors array was designed and demonstrated while integrated with compact readout electronics instrumentation. Surface topographic irregularities were simulated by confining SS316 powder against a thin glass cylinder, on which various plastic structures were fabricated. The sensors and associated electronics demonstrated the ability to detect cylindrical and linear voids with radii/widths as small as 0.55 mm and depths of 0.1 mm.

Keywords: Capacitive Imaging, Capacitive Sensors Array, High Spatial Resolution Imaging, Surface Topography, In-Situ Quality Control, Powder Bed Fusion

1. Introduction

In Powder Bed Fusion (PBF), metal powder layers are selectively melted by a laser (1) or electron beam (2). However, this discontinuous thermal process introduces challenges: thermal stress and impurities can lead to critical defects such as porosity, lack of fusion, and key holing (3; 4; 5), reducing the load-bearing area of the part and its mechanical properties (6). While traditional Non-Destructive Testing (NDT) techniques like radiography and ultrasonics are used for post-production Quality Control (QC)(6), they cannot inspect the internal structure during fabrication. X-ray microtomography offers high-resolution internal inspection but is prohibitively expensive and too slow for industrial lines (7; 8; 9). Consequently, in-situ layer-by-layer monitoring has been identified as the critical enabler for next-generation QC (10; 11). By assessing each layer during production, it becomes possible to detect defects immediately, triggering corrective actions or halting the process to prevent material waste (12). This capability is essential not only for reducing energy consumption and feedstock losses but also for process optimization and part qualification (13).

Several in-situ approaches have been explored. Optical sensors are employed to measure melt pool irradiance (14), but provide only indirect signatures of stability. Near-field microwave sensors have been applied to evaluate the adequacy of layer consolidation, however, their applicability is constrained by limited sensitivity (15). Eddy Current (EC) sensors exploit electromagnetic induction to assess conductivity differences (16; 17), with recent arrays capable of imaging layers in synchrony with the recoater (18). The methods reported to date primarily target the inspection and monitoring of the consolidated component. However, the characteristics of the powder distribution have not yet been systematically examined. Powder layer quality is a key metric related to powder spreadability and ultimately part quality (19), a low specific mass deposition rate induces pronounced superheating of the melt pool and deep penetration into the underlying layer, thereby promoting the formation of coarse, fully columnar prior grain structures (20). Conversely, a high specific mass deposition rate can lead to incomplete powder melting and reduced melt superheating, favoring the development of fine, nearly equiaxed prior grains (21).

Capacitive Imaging (CI) (22) has recently emerged as a powerful alternative, offering the potential to inspect a diverse range of materials from insulators to metallic conductors. This technique relies on generating an electric field distribution between electrodes. Variations in the part's geometry, electrical conductivity, or dielectric permittivity modify this field, which is measured as a change in capacitance (23), as presented in Fig. 1. This principle is the foundation of CI (24), a technique that offers high spatial resolution, robust sensor design flexibility, and the ability to detect both topographical and superficial defects (25). For PBF, this approach can be used to evaluate roughness and surface topography for each individual powder layer, allowing for timely corrective measures and thereby avoiding part rejection after final inspection. This work investigates the application of capacitive sensors to characterize the surface condition during the powder recoating step.

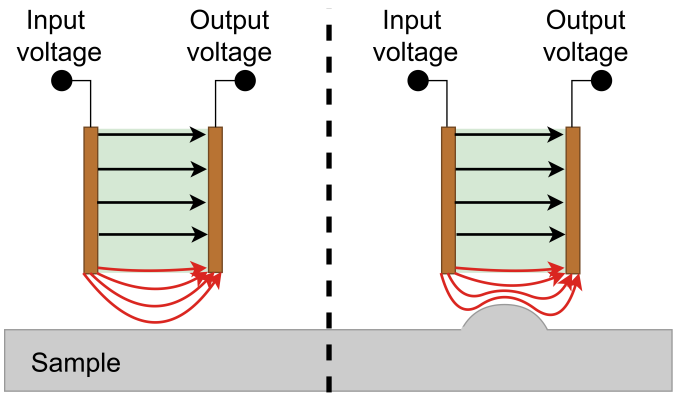

Figure 1: Schematic illustration of the operating principle of the CI, electric field fringing on a parallel plates capacitive sensor while in the presence of a topographic irregularity.

2. Capacitive Sensor and Readout Instrumentation

2.1. Sensor Electromagnetic Principle

According to electromagnetic field theory, the distribution of an electric charge relates to the resulting electric field using Gauss's law, one of Maxwell's equations. In its integral form, it can be written as (1).

$$\oint_s \vec{D} \cdot \vec{ds} = Q \tag{1}$$

where D is the electric displacement field and Q the total charge through a closed surface S that surrounds any volume. Assuming the involved materials homogeneous, isotropic, non-dispersive, and linear a simple constitutive relationship between **D** and the electric field **E**:

$$\mathbf{D} = \varepsilon \mathbf{E}(\mathbf{x}, \mathbf{y}, \mathbf{z}) \tag{2}$$

where ε denotes the dielectric permittivity of the material and $\mathbf{E}(\mathbf{x}, \mathbf{y}, \mathbf{z})$ is the electric field expressed as a spatial distribution.

The capacitive sensor maps the spatial distribution of the medium's permittivity within its sensitive zone to the capacitance value between a pair of electrodes. This is expressed in terms of the charge stored, **Q**, and the applied voltage, **V**, between the electrodes by (3):

$$C = \frac{Q}{V} \tag{3}$$

Consequently, the capacitance measured between a given sensing electrode and the excitation electrode can be expressed as in (4):

$$C = \frac{\oint_s \varepsilon \vec{\mathbf{E}}(x, y, z) \cdot \vec{ds}}{V} \tag{4}$$

When a capacitive sensor is brought into the vicinity of a metallic surface, or a surface composed of metallic particles, the free charges within the metal rearrange such that the electric field inside the metal becomes approximately zero. From the sensor perspective, the presence of the metallic surface increases the effective coupling of the electric field, leading to a higher measured capacitance. Consequently, the closer the surface is to the sensor, the larger the capacitance becomes.

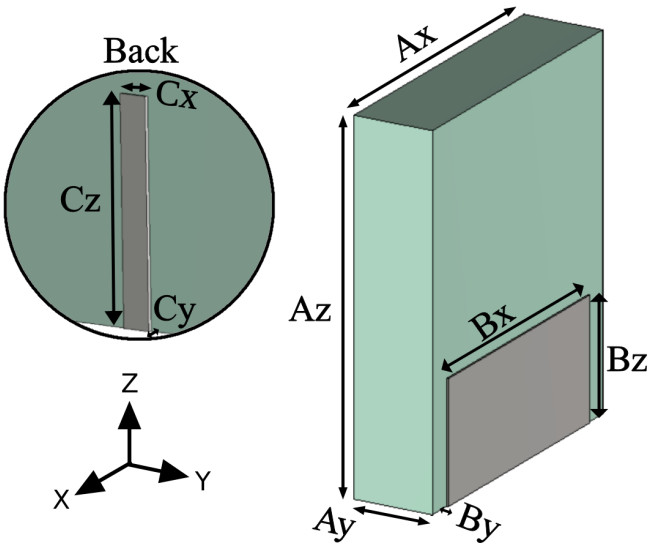

Figure 2: The developed capacitive probe in Computer Simulation Technology (CST). The sensing electrode is show in the detailed view.

Feature	X (mm)	Y (mm)	Z (mm)
Substrate (A)	6.0	1.6	7.2
Excitation (B)	5.0	0.035	2.4
Sensing (C)	0.4	0.035	2.4

Table 1: 3D model probe sensor dimension.

For metals and metal powders commonly used in powder bed fusion processes, electrical conductivity is usually higher than 3 % IACS. Under these conditions, and for the operating frequencies of the capacitive sensor, the surface can be approximated as an equipotential boundary. As a result, the sensor response is primarily sensitive to the distance between the sensor and the surface, while being only weakly dependent on the electrical conductivity.

2.2. Sensor Simulation

The capacitive sensor was modeled using the E-static module of CST Studio Suite (26). Several optimization iterations were carried out, taking into account the fabrication constraints associated with Printed Circuit Board (PCB) technology for the sensor electrode arrays. The electrostatic solver was selected, and the simulation boundaries were defined as open to ensure non-reflective behavior.

An FR-4 PCB substrate ($\epsilon = 4.3, \mu = 1$) with a thickness of 1.6 mm was selected. Both excitation and sensing electrodes were implemented in copper ($\epsilon = 1, \mu = 1$) with a thickness of 0.035 mm. Since the electrical conductivity and charge-carrying capability of metal powder is comparable to that of the resulting consolidated metal (27), the powder surface was modeled as a bulk metal. The selected material was SS316L

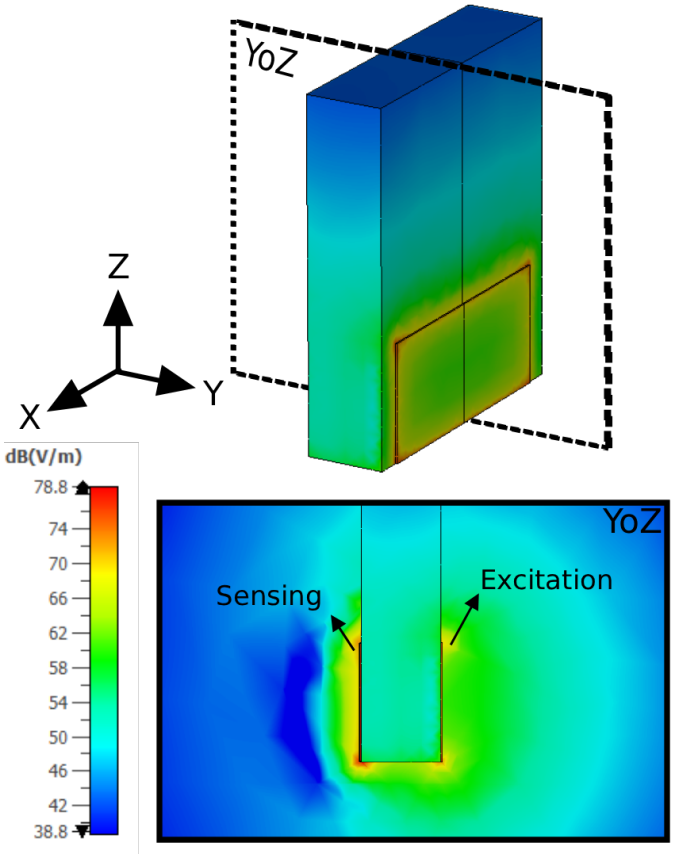

Figure 3: Sensor's electric field in the sensitive zone plotted in YoZ planes.

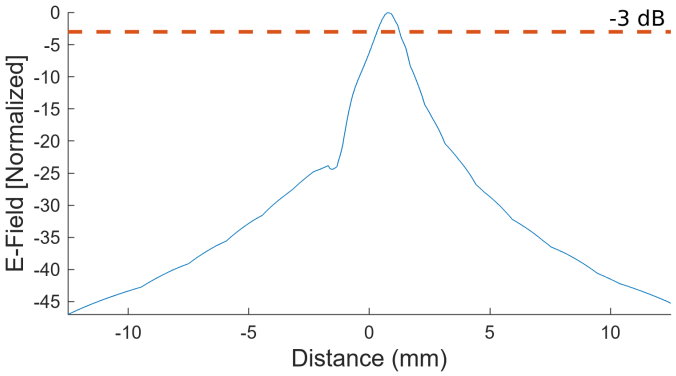

Figure 4: Electric field magnitude in through the Y axis direction.

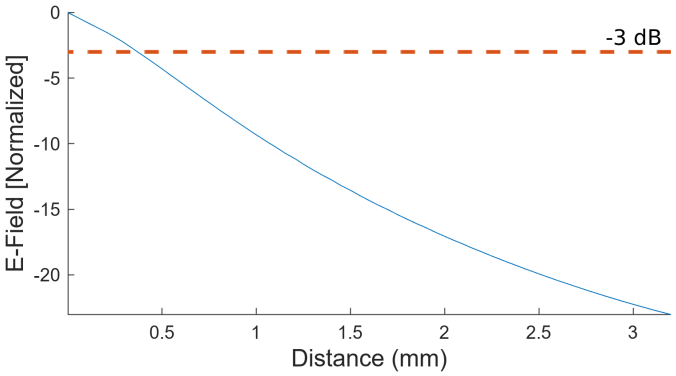

Figure 5: Electric field magnitude in through the Z axis direction.

($\epsilon = 1, \mu \approx 1$), and defects were represented as void circular regions with a radius of 1.25 mm. The model, as shown in Fig. 2 has the dimensions presented in Table 1.

As illustrated in Fig. 3, the electric field density distribution in the YoZ plane of the sensitive region exhibits a pronounced concentration directly beneath the excitation plate, which enhances the overall detection sensitivity. Subsequently, the electric field was evaluated along the y-axis at the probe center, as depicted in Fig. 4. The sensitive region reaches the -3 dB threshold at distances of 0.31 mm and 1.24 mm, respectively, implying that two distinct flaws can be reliably discriminated only if they are separated by at least 0.93 mm.

To further characterize the electric field within the sensitive region, Fig. 5 presents the field distribution along the z-axis at the center of the probe. The results indicate that the electric field decays approximately exponentially with increasing distance from the probe, reaching -3 dB threshold at a distance of 0.37 mm. This behavior suggests that the separation between the probe surface and the sample surface (lift-off) should be minimized in order to improve accuracy and sensitivity.

A parametric simulation was performed to assess the sensor's capability to detect and discriminate circular voids with a radius of 1.25 mm within a rectangular prism of dimensions 15 mm×15 mm×3 mm, assuming a lift-off distance of 0.2 mm. Figure 7 illustrates the spatial distribution of the capacitance variation when a cylindrical defect is positioned within the active region of the sensor. The simulated sensor indicates a measure capacitance of 18.91 fF in the absence of the defect and 19.82 pJ in its presence. This substantial difference demonstrates that the sensor can reliably distinguish air-filled voids from the surrounding powder medium.

Subsequently, a second parametric simulation was carried out to reproduce the laboratory conditions, as shown in Fig 6. In this configuration, a glass ($\epsilon = 6, \mu \approx 1$) layer was introduced between the probe and the sample, and the air-filled void was replaced by a plastic PLA ($\epsilon = 2.3, \mu \approx 1$) inclusion. The results of both simulations are compared in Figure 7. Due to the higher dielectric permittivity of the glass, the laboratory configuration exhibits an increased baseline capacitance, with values of 23.4 fF in the absence of the defect and 24.41 fF in its presence, while the relative capacitance variation remains comparable. Consequently, the measurements obtained under laboratory conditions are expected to be representative of those acquired in a PBF machine.

2.3. Sensor Array and Readout Instrumentation

To extend the imaging coverage, an array of sensor electrodes was employed. Specifically, twelve identical sensing electrodes were arranged in alignment, allowing the generation of twelve observation lines in a single pass of the probe. The pitch between electrodes was constrained by the PCB manufacturing clearance and was set to 0.2 mm. Measurement of the full electrode array is accomplished using a dedicated Integrated Circuit

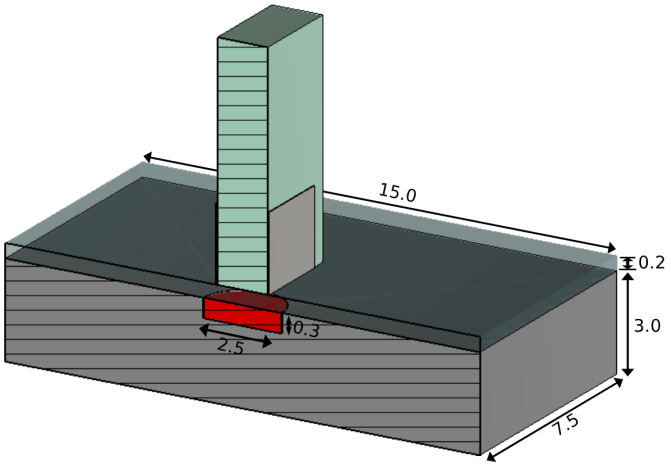

Figure 6: Three-dimensional model, sectioned in the X-plane, representing the simulation with glass and defect filled with PLA.

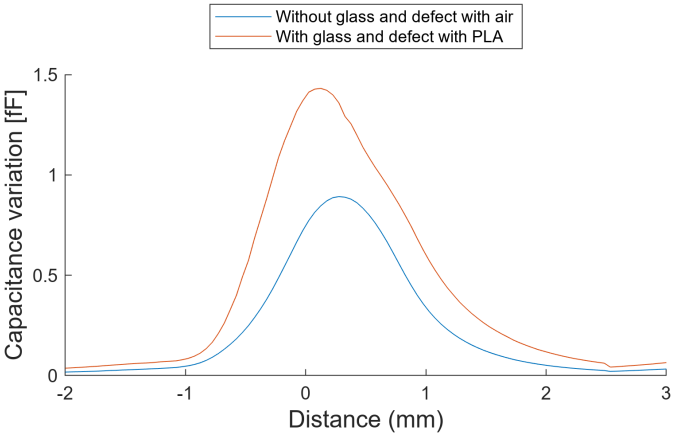

Figure 7: Capacitance measured in simulation, while the defect moving under the sensor.

(IC) that implements a capacitance-sensing technique known as the shunt method. In this approach, an excitation signal is applied to the excitation electrode, while the charge induced on the sensing electrode is converted into the digital domain using a Sigma-Delta converter. In addition to the selected Capacitance to Digital Converter (CDC) IC (AD7142), an MSP430 microcontroller is used to configure and interrogate the CDC, as well as to forward the capacitance readouts to a Personal Computer (PC).

The CDC generates a 250 kHz, 3.3 V amplitude square-wave signal as the excitation source. Capacitance measurements are performed with a resolution better than 1 fF and an update rate of 3.072 ms per sensor. A total acquisition time of 36.864 ms is required to complete a measurement across all twelve sensors. Sensor switching is accomplished via the built-in multiplexer. The resulting digital data is transferred to the MSP430 microcontroller and temporarily stored in a circular buffer while awaiting transmission to the PC through a USB-emulated UART port.

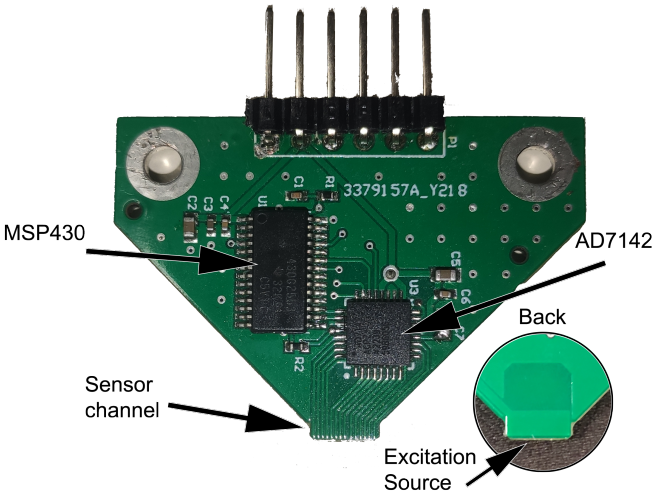

Figure 8: Developed capacitive probe.

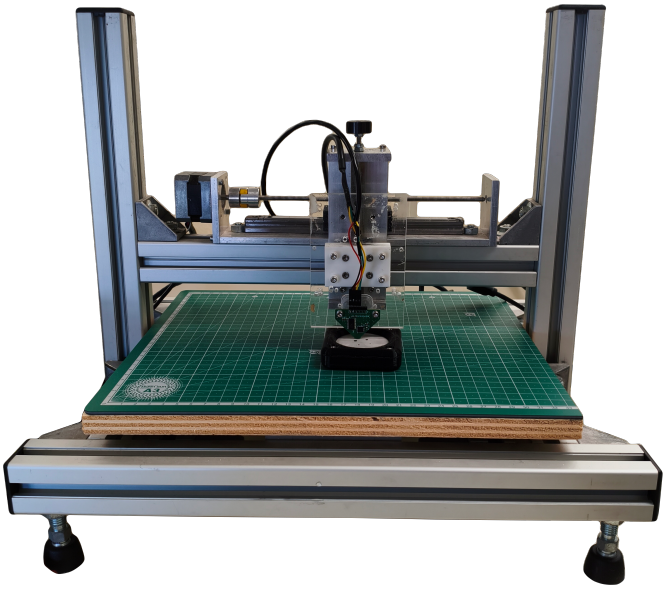

Figure 9: Experimental setup used for the capacitive imaging technique.

3. Experimental Results

3.1. Pilot Installation

An internally developed XYZ benchtop gantry system with a spatial resolution of 0.05 mm was used to move the prototyped sensor array across the sample surface. A Python-based Graphical User Interface (GUI) communicates with both the MSP430 microcontroller and the XY positioning controller via USB. The GUI simultaneously acquired data from the MSP430 and issued motion commands to the XY stage. MATLAB was then used to convert the acquired signals into capacitance measurements and to perform basic calibration.

Because it is difficult to reproducibly create and maintain inhomogeneities in the powder across repeated measurements, a dedicated methodology and mockup were developed to fabricate controlled test samples. The powder is confined within

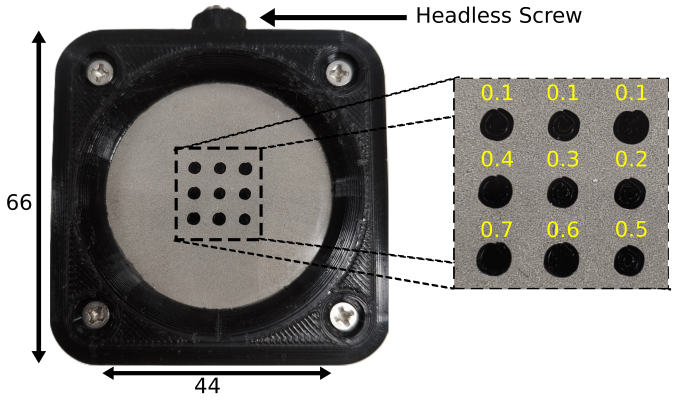

(a) 3×3 array of nine circular features with differents heights.

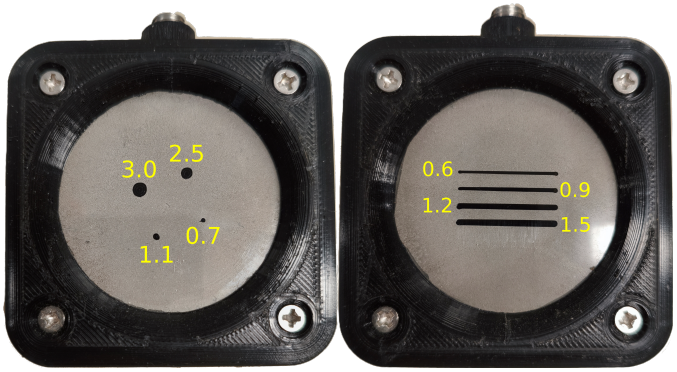

(b) Four circular features with differents diameter.

(c) Four linear features with differents thickness.

Figure 10: Manufactured samples to simulate a specific flaw in the powder, filled with stainless steel 316 powder. Measures in millimeter.

a plastic 3D printed PLA holder that incorporates a 0.2 mm thick glass window. Surface irregularities are intentionally introduced by 3D printing PLA features directly onto the inward-facing side of the glass, i.e., the side in contact with the powder. After fabrication, the glass is mounted onto the holder, the powder is filled in, and the assembly is tightly sealed using a headless screw.

This approach, however, introduces several deviations from the final testing conditions, namely the additional thickness of the glass layer, the presence of the glass itself (whose dielectric constant is higher than that of air), and the incorporation of PLA features (also with a higher dielectric constant than air) to emulate the inhomogeneities. These modifications are expected to influence the experimental results, as they reduce the electromagnetic contrast at the powder surface and may therefore limit the achievable measurement sensitivity.

The first sample, shown in Fig. 10a, consists of a 3×3 array of nine circular features, each separated from its neighbors by 2.5 mm, radii of 1.25 mm and heights/depth as specified in figure. The sample illustrated in Fig. 12 comprises four circular features with diameter 3 mm, 2.5 mm, 1.1 mm and 0.7 mm, and height/depth of 0.1 mm. Finally, the sample depicted in Fig. 10c contains four 20 mm line features, with widths 1.5 mm, 1.2 mm, 0.9 mm and 0.6 mm, and height/depth of 0.1 mm.

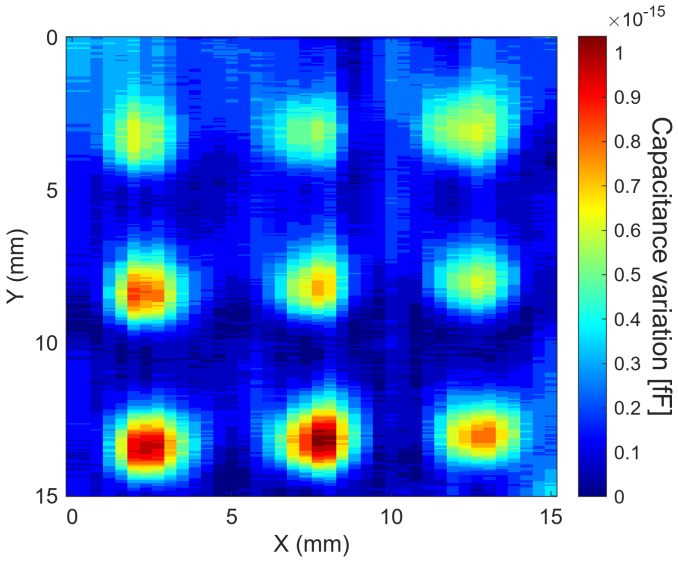

Figure 11: Capacitive imaging of the nine circular features sample. The experiments were performed with 0.2 mm lift-off.

3.2. *Experiments*

First experiment was conducted to evaluate the capability of detecting inhomogeneities with different heights. Five linear scans were made to acquire a $15mm \times 15mm$ CI over the sample presented in Fig. 10a, with a step of 0.05 mm and lift-off distance of 0.2 mm. The CI acquired is shown in Fig. 11. As expected CI over the shallower inhomogeneities has lower Signal to Noise Relation (SNR), although it is still possible its clear identification.

The following experiment was conducted to assess the spatial resolution of the probe and its capability to detect small inhomogeneities within the powder. A scan covering an area of $15cm \times 17cm$ was performed over the sample shown in Fig. 10b, using a step size of 0.05 mm and a lift-off distance of 0.2 mm. The resulting data are presented in Fig. 12. The inhomogeneities with radii of 3 mm, 2.5 mm and 1.1 mm exhibit a high SNR and are clearly visible. The smallest void, with a radius of 0.7 mm, produces a weaker signal amplitude, and its identification is further compromised by the slight non-flatness observed in the holder glass. It should also be noted that, due to the probe width, the scan in the X direction could not be further extended to include additional margin around the smallest defect.

Finally a scan over the sample presented in Fig. 10c was made to validate the detection of line inhomogeneities. The parameters of the scan were equal to the second experiment, and the acquired CI is shown in Fig. 13

To enable a quantitative comparison between the experimental and simulated results, the three-centered circular feature was modeled in CST. As shown in Fig. 14, the capacitive variations observed in the measurements are consistent with those predicted by the simulations. The probe exhibited comparable responses regardless of the defect depth; nevertheless, the sensitivity remains sufficient to reliably discriminate between the powder and the plastic.

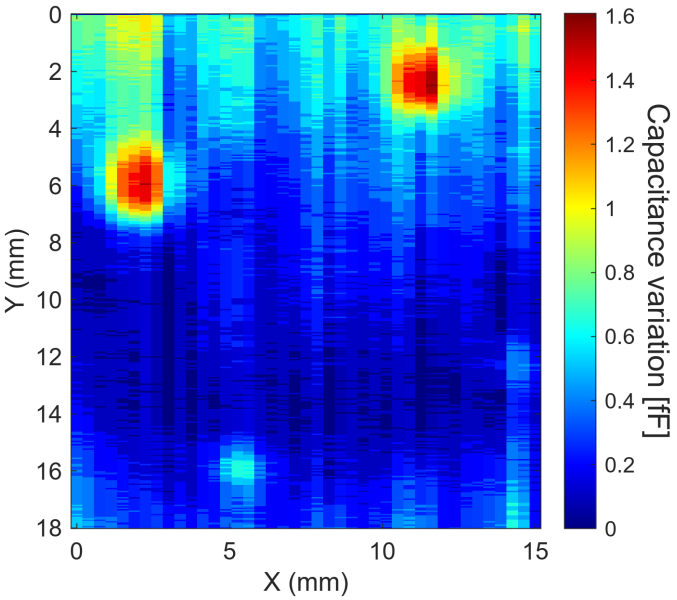

Figure 12: Capacitive imaging of the four circular features sample. The experiments were performed with 0.2 mm lift-off.

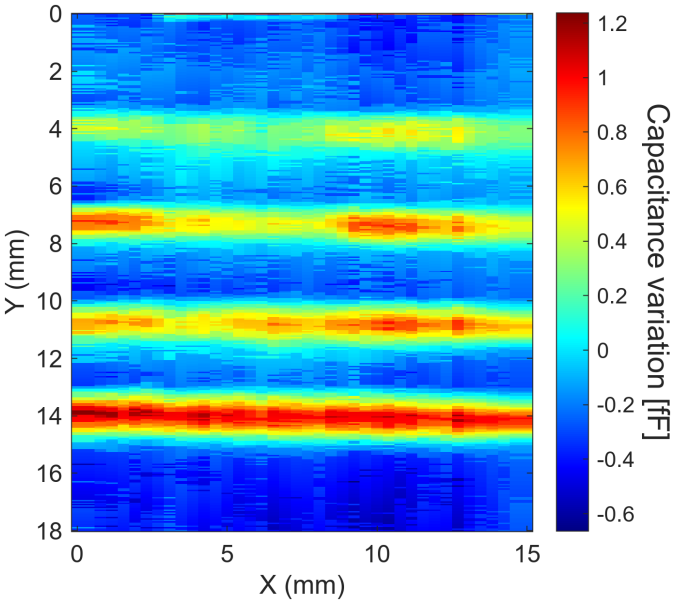

Figure 13: Capacitive imaging of the four lines sample. The experiments were performed with 0.2 mm lift-off.

To quantitatively assess image quality, the SNR and sensitivity parameters were evaluated. The SNR was determined by defining two distinct regions of interest, each comprising each spanning an area of $N \times M$ pixels: a feature region (Pf) and a defect-free background region (Pb). The effective signal contrast was calculated using Equation 5:

$$Signal = \frac{1}{N \times M}\left(\sum_{i=1}^{N}\sum_{j=1}^{M} Pf_{ij} - \sum_{i=1}^{N}\sum_{j=1}^{M} Pb_{ij}\right) \quad (5)$$

The background noise, defined as the standard deviation of the pixel intensities within the defect-free region, was computed

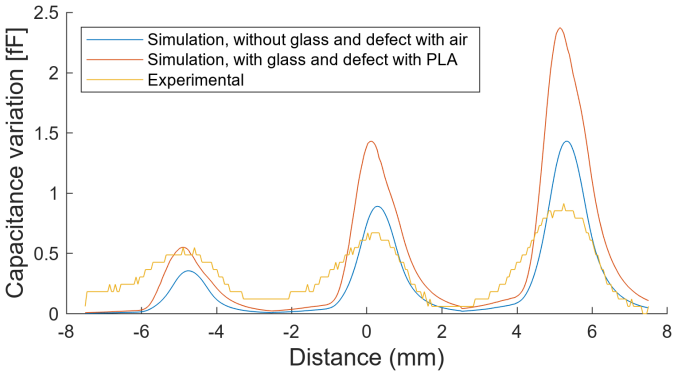

Figure 14: Capacitive variance of the three center circular features.

Sample	Feature Size	Parameters	
A	Depth (mm)	SNR	Signal (fF)
	0.1	9.79	0.59
	0.4	11.01	0.85
	0.3	10.13	0.73
	0.2	10.13	0.73
	0.7	11.77	0.98
	0.6	12.01	1.06
	0.5	11.36	0.79
B	Radius (mm)	SNR	Signal (fF)
	3	12.45	0.61
	2.5	11.90	0.67
	1.1	6.86	0.24
	0.7	2.93	0.06
C	Thickness (mm)	SNR	Signal (fF)
	0.6	16.14	0.53
	0.9	19.20	0.83
	1.2	21.53	0.90
	1.5	23.77	1.30

Table 2: SNR values for each of the scanned features

according to Equation 6:

$$Noise = \sqrt{\frac{1}{N \times M}\sum_{i=1}^{N}\sum_{j=1}^{M}(Pb_{ij} - \bar{Pb})^2} \quad (6)$$

where $\bar{Pb}$ denotes the mean pixel intensity of the background region. Finally, the SNR was derived using Equation 7, with the resulting values summarized in Table 2.

$$SNR = 10 \times \log_{10}\left(\frac{Signal}{Noise}\right) \quad (7)$$

4. Conclusion

This work demonstrates the feasibility of capacitive imaging for topographic characterization of powder layers in powder bed fusion additive manufacturing. Finite element modeling supported the selection and optimization of the electrode

geometry, enabling the design of a compact 12-sensor array compatible with PCB fabrication constraints and high-density integration. The developed probe, combined with dedicated readout electronics, achieved high acquisition speed and fF resolution, supporting layer-by-layer inspection concepts suitable for recoater-mounted deployment.

The results demonstrated reliable detection of sub-millimeter inhomogeneities width depths as small as 0.1 mm. Although convenient for the intended purpose, the adopted sample fabrication methodology limits the demonstrated sensor performance, which is expected to be substantially better under real operating conditions. Overall, the reported results support capacitive sensor arrays as a promising candidate for in-situ, layer-wise surface monitoring in powder bed fusion, offering a non-optical, low-cost, and scalable alternative for early detection of powder recoating anomalies.

Future work will focus on implementing the probe directly on a recoater system to perform real-time, in-situ measurements of successive powder layers during part production. Scaling the system to larger sensor arrays with parallel readout channels is another key direction, enabling full-width, layer-by-layer inspection. Additionally, combining capacitive imaging with complementary sensing modalities—such as optical or eddy current monitoring—should be explored to develop multi-physics, in-situ quality control platforms with enhanced detection reliability and improved characterization of powder recoating irregularities.

CRediT authorship contribution statement

Victor Macedo: Writing – original draft, Validation, Investigation, Data curation, Formal analysis, Software. **Jorge Assis**: Writing – review & editing, Investigation. **André Barrancos**:Software, Writing – review & editing, Investigation.**Luís S. Rosado**: Writing – review & editing, Validation, Supervision, Investigation, Funding acquisition, Conceptualization, Project administration.

Declaration of competing interest

The authors declare that they have no known competing financial interests or personal relationships that could have appeared to influence the work reported in this paper.

Acknowledgements

This work is funded by national funds through FCT – Fundação para a Ciência e a Tecnologia, I.P., and, when eligible, co-funded by EU funds under project/support UID/50008/2025 – Instituto de Telecomunicações, with DOI identifier - https://doi.org/10.54499/UID/50008/2025. The authors would like to express their gratitude to DEEC from IST for the financial support of the temporary bridging scholarships program.

Data availability

Data will be made available on request.

References

[1] D. Wyszynski, M. Grabowski, Chapter 9 - Powder bed fusion, in: J. Izdebska-Podsiadły (Ed.), Polymers for 3D Printing, Plastics Design Library, William Andrew Publishing, 2022, pp. 105–112. doi:10.1016/B978-0-12-818311-3.00001-X.

[2] A. Margueret, P. Lhuissier, G. Martin, In situ recrystallization of pure Cu during electron beam powder bed fusion, Additive Manufacturing Letters 15 (2025) 100329. doi:10.1016/j.addlet.2025.100329.

[3] D. D. Gu, W. Meiners, K. Wissenbach, R. Poprawe, Laser Additive Manufacturing of Metallic Components: Materials, Processes and Mechanisms, International Materials Reviews 57 (3) (2012) 133–164. doi:10.1179/1743280411Y.0000000014.

[4] J. Braun, L. Kaserer, J. Stajkovic, K. H. Leitz, B. Tabernig, P. Singer, P. Leibenguth, C. Gspan, H. Kestler, G. Leichtfried, Molybdenum and Tungsten Manufactured by Selective Laser Melting: Analysis of Defect Structure and Solidification Mechanisms, International Journal of Refractory Metals and Hard Materials 84 (2019) 104999. doi:10.1016/j.ijrmhm.2019.104999.

[5] M. Yang, A. Rezaei, M. Vlasea, Process screening in additive manufacturing: Detection of keyhole mode using surface topography and machine learning, Additive Manufacturing Letters 13 (2025) 100275. doi:10.1016/j.addlet.2025.100275.

[6] C. Mandache, Overview of Non-Destructive Evaluation Techniques for Metal-based Additive Manufacturing, Materials Science and Technology 35 (9) (2019) 1007–1015. doi:10.1080/02670836.2019.1596370.

[7] S. Patel, H. Chen, M. Vlasea, Y. Zou, The influence of beam focus during laser powder bed fusion of a high reflectivity aluminium alloy — AlSi10Mg, Additive Manufacturing 59 (2022) 103112. doi:10.1016/j.addma.2022.103112.

[8] C. Pauzon, R. Daudin, P. Lhuissier, X. Bataillon, P. Lapouge, P. Hébrard, P. Peyre, F. Coste, L. Varoto, E. Boller, J.-J. Blandin, In situ porosity imaging with synchrotron X-ray tomography during laser rescanning of Zr-based metallic glass by laser powder bed fusion, Additive Manufacturing Letters 15 (2025) 100318. doi:10.1016/j.addlet.2025.100318.

[9] T. Menaria, M. Kumar, Review on Radiographic Imaging Modalities for Non-destructive Testing and Evaluation (NDT & E) (Mar. 2019). doi:10.2139/ssrn.3356362.

[10] D. Y. Kononenko, V. Nikonova, M. Seleznev, J. van den Brink, D. Chernyavsky, An in situ crack detection approach in additive manufacturing based on acoustic emission and machine learning, Additive Manufacturing Letters 5 (2023) 100130. doi:10.1016/j.addlet.2023.100130.

[11] P. Charalampous, I. Kostavelis, D. Tzovaras, Non-destructive quality control methods in additive manufacturing: a survey, Rapid Prototyping Journal 26 (4) (2020) 777–790. doi:10.1108/RPJ-08-2019-0224.

[12] M. Hirsch, R. Patel, W. Li, G. Guan, R. K. Leach, S. D. Sharples, A. T. Clare, Assessing the Capability of In-situ Nondestructive Analysis During Layer Based Additive Manufacture, Additive Manufacturing 13 (2017) 135–142. doi:10.1016/j.addma.2016.10.004.

[13] C. Kube, Y. Shu, A. Lew, D. Galles, Real-time Characterization of Laser-Generated Melt Pools Using Ultrasound, Materials Evaluation 76 (Apr. 2018).

[14] M. Grasso, B. M. Colosimo, Process Defects and *In Situ* Monitoring Methods in Metal Powder Bed Fusion: a Review, Measurement Science and Technology 28 (4) (2017) 044005. doi:10.1088/1361-6501/aa5c4f.

[15] A. Barancos, V. Macedo, R. L. Batalha, M. A. Machado, T. G. Santos, L. S. Rosado, Experiments with Near-Field Microwave Imaging for Powder Bed Fusion Metal Additive Manufacturing, Research and Review Journal of Nondestructive Testing 1 (1) (Aug. 2023). doi:10.58286/28139.

[16] R. Saddoud, K. Perlin, N. Sergeeva-Chollet, T. Delacroix, A. Skarlatos, J. P. Garandet, On the potential of eddy current characterization of the ferritic content of recovered 316L powders after LaserPowder bed fusion fabrication, Additive Manufacturing Letters 9 (2024) 100207. doi:10.1016/j.addlet.2024.100207.

[17] A. Barrancos, R. L. Batalha, L. S. Rosado, Towards enhanced eddy current testing array probes scalability for powder bed fusion layer-wise imaging, Sensors 23 (5), number: 2711 tex.pubmedid: 36904914 (2023). doi:10.3390/s23052711.

[18] P. Faria, R. L. Batalha, A. Barrancos, L. S. Rosado, On-line Quality Control of Powder Bed Fusion with High-Resolution Eddy Current Testing Inductive Sensor Arrays, Sensors 24 (21) (2024) 6827. doi:10.3390/s24216827.

[19] M. A. Spurek, F. Sillani, L. Haferkamp, E. Tosoratti, A. B. Spierings, C. M. Magazzeni, M. Meisnar, K. Wegener, Effect of powder properties, process parameters, and recoating speed on powder layer properties measured by in-situ laser profilometry and part properties in laser powder bed fusion, Additive Manufacturing 95 (2024) 104512. doi:10.1016/j.addma.2024.104512.

[20] H. Z. Fu, L. Liu, Progress of Directional Solidification in Processing of Advanced Materials, Materials Science Forum 475-479 (2005) 607–612. doi:10.4028/www.scientific.net/MSF.475-479.607.

[21] T. Wang, Y. Y. Zhu, S. Q. Zhang, H. B. Tang, H. M. Wang, Grain morphology evolution behavior of titanium alloy components during laser melting deposition additive manufacturing, Journal of Alloys and Compounds 632 (2015) 505–513. doi:10.1016/j.jallcom.2015.01.256.

[22] G. Diamond, D. A. Hutchins, A New Capacitive Imaging Technique for NDT, Sensors 2024 (2006).

[23] S. Everton, P. Dickens, C. Tuck, B. Dutton, Identification of Sub-surface Defects in Parts Produced by Additive Manufacturing, Using Laser Generated Ultrasound, Mater. Sci. Technol 1 (2019) 141–148.

[24] X. Hu, W. Yang, Planar Capacitive Sensors – Designs and Applications, Sensor Review 30 (1) (2010) 24–39. doi:10.1108/02602281011010772.

[25] X. Yin, D. Hutchins, Non-destructive evaluation of composite materials using a capacitive imaging technique, Composites Part B: Engineering 43 (3) (2012) 1282–1292. doi:https://doi.org/10.1016/j.compositesb.2011.10.018.

[26] CST Studio Suite (Jul. 2023).
URL `https://www.3ds.com/products/simulia/cst-studio`

[27] V. Macedo, A. Barancos, M. A. Machado, T. Santos, T. G. Santos, L. S. Rosado, Evaluating Capacitive Imaging for Powder Bed Fusion Metal Additive Manufacturing, Research and Review Journal of Nondestructive Testing 1 (1) (Aug. 2023). doi:10.58286/28140.